applied sciences

MDPI

Article

Microchannel-Embedded D-Shaped Photonic Crystal Fiber-Based Highly Sensitive Plasmonic Biosensor

Jannatul Mawa Nijhum [1], Tanvir Ahmed [1,*], Md. Anwar Hossain [2], Javid Atai [3] and Nguyen Hoang Hai [4]

[1] Department of Electrical and Electronic Engineering, Rajshahi University of Engineering & Technology (RUET), Rajshahi 6204, Bangladesh; jannatulnijhumeee@gmail.com
[2] Department of Electrical and Electronic Engineering, Bangladesh University of Business and Technology (BUBT), Dhaka 1216, Bangladesh; anwar.ee113@ieee.org
[3] School of Electrical and Information Engineering, The University of Sydney, Sydney, NSW 2006, Australia; javid.atai@sydney.edu.au
[4] School of Electronics and Telecommunication, Hanoi University of Science and Technology, Hanoi 100000, Vietnam; hai.nguyenhoang@hust.edu.vn
* Correspondence: tanvir_eee_ruet@yahoo.com

Abstract: An improved design of a D-shaped photonic crystal fiber (PCF)-based refractive index (RI) sensor is proposed that uses the surface plasmon resonance phenomenon. The sensor consists of a large semicircular open channel that is inserted at the upside of the D-shaped PCF. A thin plasmonic sensing layer is deposited on the interior surface of the channel to excite the surface plasmon wave that eliminates the requirement of additional effort to fabricate a well-polished sensing layer of the D-shaped sensor. The sensor's optical properties are numerically explored by the finite element method. The sensor is optimized to detect the RI of biological and biochemical analytes in the range of 1.33 to 1.44, shows spectral sensitivity as high as 63,000 nm/RIU with a spectral resolution of 1.59×10^{-06} RIU, and maximum amplitude sensitivity of 1439 RIU^{-1} with a resolution of 6.94×10^{-06} RIU. It is also found that the sensor's linearity parameter is very high with a large figure of merit of about 839. Additionally, the sensor's fabrication tolerance is studied by varying its structural parameters. Therefore, high sensing parameters with a wide detection range make this microchannel-based D-shaped PCF sensor an appropriate device for the application of biological and biochemical analyte detection.

Keywords: D-shaped PCF; microchannel; optical fibers for sensing; surface plasmon resonance

Citation: Mawa Nijhum, J.; Ahmed, T.; Hossain, M.A.; Atai, J.; Hai, N.H. Microchannel-Embedded D-Shaped Photonic Crystal Fiber-Based Highly Sensitive Plasmonic Biosensor. *Appl. Sci.* **2022**, *12*, 4122. https://doi.org/10.3390/app12094122

Academic Editor: Agnese Magnani

Received: 13 March 2022
Accepted: 15 April 2022
Published: 19 April 2022

1. Introduction

Surface plasmon polaritons (SPPs) are propagating electromagnetic waves that include plasma oscillations of negatively charged particles in metal and lightwave in dielectric/air. In recent years, SPP-based optoelectronic devices have received a lot of interest for their ability to detect a very little variation of analyte refractive index (RI) and provide high sensitivity, immunity to electromagnetic interference, label-free and real-time detection [1,2]. The surface plasmon resonance (SPR) occurs at a particular frequency (i.e., resonant wavelength) and similar polarization state when the surface plasmon (SP) is excited by the evanescent electric field and the input-guided lights are phase matched. The resonant wavelength of the SPR-based sensing device is extremely responsive to the analyte in contact and a little alteration of the sensing medium RI results in resonant wavelength shifting; therefore, a qualitative measure of the wavelength shift allows to track unknown analyte RI. Different optical structures, for example, the prism-based structure proposed by Otto and Kretschmann–Raether, fiber Bragg grating, optical fiber, or microstructured optical fiber, are used that increase the momentum of the light to excite SPPs at the metal–dielectric/metal–air boundary by evanescent wave [3]. The mechanical components of the prism-based sensors are larger in size and associated with moving parts, which limits

their applications for the remote sensing operation. Optical fiber-based sensors have great advantages over the prism-based sensors for their small size, flexible nature, and remote sensing operation [4,5]. For example, an SPR-based optical-fiber sensor with metallic grating is shown in [4] with a maximum sensitivity of 25 μm/RIU for RI sensing range from 1.33 to 1.38. However, limited structural parameters of these sensors prohibit their wider operations, and to work as a sensor, cladding needs to be removed. Among different SPR-based sensing configurations, the SPR integrated photonic crystal fiber (PCF) sensors allow endless ways to couple strongly core-guided light with the SP by reshaping structural parameters based on sensing applications and overcome the limitations of conventional systems [6,7]. Due to miniaturization, real-time sensing, flexible design, and remote sensing properties, PCF-based SPR sensors can be applied for many useful sensing applications [7–9]. The operation of the PCF-based SPR sensors is primarily classified depending on the material deposition either outside on the dielectric of PCF or inside the airhole wall of PCF. Metal layer deposition on the internal wall of PCF leads to good detection of analyte due to easy coupling of the core mode with SPP mode [10]. However, metal deposition on the wall of a tiny air hole and infiltration of liquid analyte is laborious. On the other hand, metal film deposition over the dielectric surface of PCF makes the sensor fabrication easier, which opens the possibility of novel designs of PCF sensors such as D-shaped sensors, exposed-core sensors, U-shaped sensors, and so on [11–13]. The selection of plasmonic metal is crucial to improve the sensitivity of these sensors. Silver, aluminum, copper, and gold are frequently used as sensing media [14]. Though silver has lower optical damping and a narrow loss spectrum, it exhibits oxidation difficulty in the surroundings aqueous medium [15]. Gold shows superior performance among all these metals due to being chemically inert, biocompatible, having larger peak shift, and being stable in an aqueous environment [14,16].

Most of the substances of interest have an RI less than 1.40. Different biological and chemical samples have an RI in the range of 1.40 to 1.44 [17,18]. For example, the RI of kerosine is 1.44, different alcohols have higher RI, such as 1-hexanol which has an RI of 1.416 and 4-methyl-2-pentanol which has an RI of 1.41. Moreover, mammalian (e.g., bovine, porcine, canine, and human) tissues have RIs higher than1.40. For example, the human kidney has an RI of 1.417, and the bovine muscle has an RI of 1.41.

In recent years, intensive efforts have been devoted towards designing D-shaped PCF sensors because they enhance the sensing performance as the energy transfer increases from core to plasmonic mode due to a closer distance between the plasmonic film and core of the PCF [19]. To fabricate the D-shaped PCF sensors, a portion of PCF is polished by the side-polishing process, and the plasmonic film is placed over the flat surface [19]. For example, a flat surface-based D-type PCF sensor with a hollow core was proposed in [20] and using spatially distributed bimetallic layers was proposed in [21]. However, a deep polishing depth increases the fragility of the PCF, and the flat surface of D-type PCF needs to be smooth, otherwise a nonuniform sensing surface arises that affects sensing performance. The sensing performance increases significantly by introducing a microchannel in the PCF sensor because of the reduction in separation of the sensing layer and core region. For example, a microchannel-based D-shaped sensor showed maximum sensitivity of 27,800 nm/RIU for RI range of 1.37 to 1.41 [22]. A hexagonal lattice D-shaped PCF sensor containing an open ring channel was proposed in [12] that can detect RI from 1.20 to 1.29 with a low wavelength sensitivity of 11,055 nm/RIU. This sensor requires extra care to make a D-shape, otherwise at the stage of the side-polishing process of the PCF side, air holes of the open ring may be damaged. A PCF sensor with two microchannels was designed to detect RI from 1.23 to 1.29 with a maximum sensitivity of 13,000 nm/RIU [23]. The problem with the sensor is that double sides of the PCF need side polishing to obtain a D-shape with microchannels on both sides of the PCF. Moreover, the sensor has low sensitivity and a low detection range. Microchannels not only improve the performance of the D-shaped sensors but also boost the sensing performance of the circular-shaped PCF sensors. For example, a U-shaped microchannel in a circular-shaped PCF next to the core

showed maximum sensitivity of 66,000 nm/RIU and a wider sensing range [13]. However, the problem of the microchannel-embedded PCFs is the difficulty of the fabrication of the channel by using a focused ion beam or laser micromachining process. The sensing layer can also be placed close to the core in the case of exposed core grapefruit fiber-based sensors to increase performance [24–26]. Additionally, in suspended core microstructured-fiber, the sensing layer is close to the core that can detect multi analyte [27]. Besides SPR-based RI sensors, other new RI sensors such as long-range SPP and Bloch surface wave based sensors are proposed to detect RI effectively [28,29].

The aim of this work is to detect a wide range of analyte RI with very high sensitivity by incorporating the benefits of a D-shaped PCF sensor and avoiding its surface roughness effect. Therefore, an improved design of a D-shaped PCF-based SPR sensor is proposed in this work with a large semicircular open channel. The construction of the novel D-shaped PCF sensor is easier because of its hexagonal lattice structure. The channel open-up process can be completed along with the fabrication of D-shaped PCF by the side-polishing method. To avoid the fragility of the PCF, we use a shallow polishing depth. Plasmonic material gold is deposited on the interior surface of the large semicircular channel. Since the plasmonic layer is deposited inside the curved channel, we can ignore the surface roughness effect of the D-shaped PCF on the sensing performance. Due to the poor adhesion of gold with the background silica, a thin adhesive coating of TiO_2 is placed over the curved surface of the channel. Numerical analysis shows that the PCF-based sensing device has a wider detection range of analytes with wavelength sensitivity of 63,000 nm/RIU and maximum amplitude sensitivity of 1439 RIU^{-1}. The large semicircular-shaped channel provides quick infiltration of analyte and effortless cleaning of the channel.

2. The Structure of the Sensor

The illustration of the proposed PCF-based plasmonic biosensor is demonstrated in the transverse plane in Figure 1a that contains silica as background material. The refractive index n as a function of wavelength λ of the PCF background material silica is evaluated by the following Sellmeier equation:

$$n^2(\lambda) = 1 + \frac{A_1\lambda^2}{\lambda^2 - B_1} + \frac{A_2\lambda^2}{\lambda^2 - B_2} + \frac{A_3\lambda^2}{\lambda^2 - B_3}. \quad (1)$$

The values of the coefficients A and B in Equation(1) are the same as those in [30]. In the proposed PCF, four air-hole layers are organized in a hexagonal lattice with an optimized pitch constant Λ = 2 μm. The stack preform of the PCF is shown in Figure 1b. Figure 1b shows that selected air holes around the center are replaced by silica's solid rods to form a single core and leakage path for light to create an evanescent electric field that reaches the plasmonic material to excite free electrons. Figure 1 shows that a microchannel with a larger air hole of diameter $d_{ch} = 2.2\Lambda$ is inserted in the PCF to contain the analyte. The air holes with a shrunk diameter $d_s = 0.6\Lambda$ and enlarged diameter $d_1 = 0.9\Lambda$ control the interaction of light with the plasmonic film and the analyte channel. All other air holes in the PCF have a diameter $d = 0.8\Lambda$. It should be noted that the structural parameters used in the model are optimized to detect analyte RI from 1.33 to 1.44 with very high sensitivity. The preform structure shows that a thick silica tube is used for the smallest air hole, and thin silica tubes are used for the larger air holes. The dimensions of air holes considered in this model are larger than the smallest air hole of the PCF fabricated in Ref. [31]. Therefore, the stack preform of the hexagonal lattice-based proposed sensor indicates that the manufacturing process of PCF can be achieved by following the stack-and-draw fiber drawing technique [31].

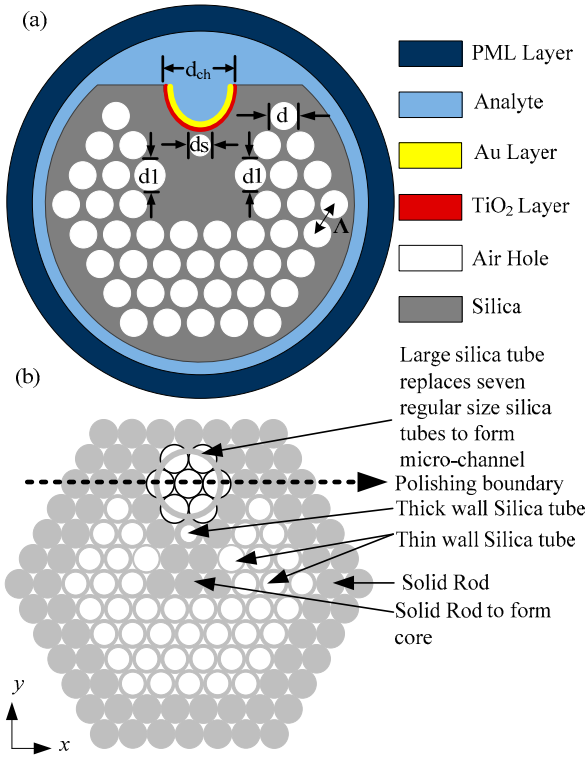

Figure 1. (**a**)Schematic view of PCF -based SPR sensor, and (**b**) Fiber's stack preform in the *x*–*y* plane.

In order to easily fill up the analyte into the microchannel, the PCF is polished by side-polishing technique as described in Ref. [19], starting from the top of the PCF to the polishing boundary as shown in Figure 1b, which leads to the formation of the D-shaped PCF sensor and opens a microchannel. The wider channel reduces the distance between the core of the PCF and the plasmonic film that leads to the strong resonance and efficient energy exchange of the coupled modes. After opening the microchannel, 6 nm of TiO_2 is deposited inside the open channel to work as an adhesive layer, and on top of that, 40 nm gold is deposited as a plasmonic medium. In this modified D-shaped PCF sensor, the flat surface is not required to be smooth because the plasmonic layer (gold) is deposited on the inner plane of the larger air hole. Moreover, the inner wall of the larger air hole has a smooth surface by itself; therefore, no additional efforts are necessary to make the sensing layer smooth, such as in the case of the flat surface of a D-shaped sensor. A high-quality thin film of the plasmonic and adhesive layer can be deposited inside the open-air hole by using physical vapor deposition (e.g., sputtering, electron beam evaporation) and chemical vapor deposition process (e.g., atomic layer deposition) [32,33]. Moreover, a long-lasting immobilized uniform gold layer can be deposited by using the nano particle-layer-deposition (NLD) process, even in the case of uneven circular silica capillary [34]. In addition, the Tollens' reaction chemical coating method can be used to deposit metal in the inner plane of the open channel [35]. The permittivity of gold is found by the following the Drude–Lorentz model:

$$\varepsilon_{Au} = \varepsilon_{\infty} - \frac{\omega_D^2}{\omega(\omega + j\gamma_D)} - \frac{\Delta\varepsilon\Omega_L^2}{(\omega^2 - \Omega_L^2) + j\Gamma_L\omega} \tag{2}$$

where ω is the angular frequency. The other parameters in Equation (2) can be found from [36]. The RI of adhesive layer TiO_2 is found from [37] as follows:

$$n^2(\lambda) = 5.913 + \frac{2.441 \times 10^7}{\lambda^2 - 0.803 \times 10^7}. \tag{3}$$

The PCF has a finite number of air holes in the cladding that result in power loss from the core of the PCF. The loss of fundamental mode during propagation is computed by the following equation:

$$\alpha(\mathrm{dB/cm}) = -8.686 \times \kappa_0 \mathrm{Im}(n_{eff}) \times 10^4 \quad (4)$$

where $\kappa_0 = 2\pi/\lambda$ represents the free space wave number, and $\mathrm{Im}(n_{eff})$ indicates the imaginary component of effective RI of the fundamental mode [11].

3. Performance Analysis and Numerical Results

To numerically explore the optical properties of the proposed sensor, finite element method (FEM)-based commercial software COMSOL Multiphysics is used. For computational purposes, we use a circular perfectly matched boundary to attenuate all electromagnetic radiation that arrives at the boundary. Maximum mesh size is found by $\lambda/6n$ for the entire geometry, where n is the mesh size parameter that increases up to 1 and λ is the operating wavelength. Figure 2 shows the confinement loss and the maximum number of elements as a function of n. In this model, the region of silica is much larger compared with the air-gap regions. From Figure 2, it can be seen that confinement loss remains almost constant for n< 0.6. Therefore, to make the computation process faster, we use 100,168 elements.

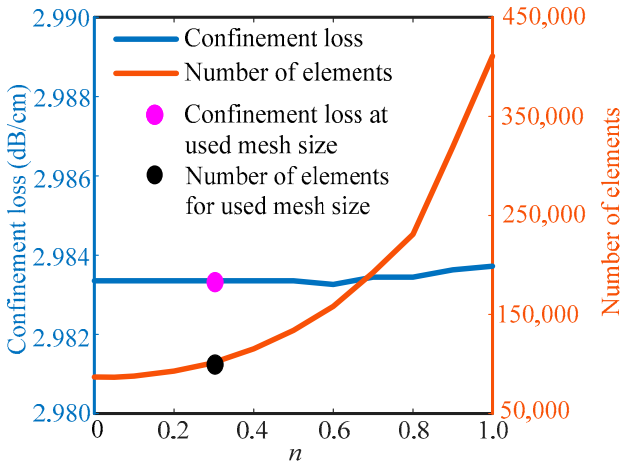

Figure 2. Confinement loss and maximum number of elements as a function of mesh size parameter.

Asymmetrical structure of the PCF results in the existence of birefringence. Therefore, light propagating inside the fiber shows x-and y-polarizations of the fundamental and SPP modes, as shown in Figure 3a–d.The field distribution of these modes is shown for the analyte RI = 1.43 at the resonant wavelengths. Figure 3e demonstrates the RI and confinement loss as a function of wavelength for the fundamental and the SPP modes for both x- and y-polarizations. It is seen that resonance occurs at the phase-matching wavelength that results in maximum energy transfer from the fundamental modes to the SPP modes, and confinement loss becomes maximum for both polarized lights. For example, phase matching or resonant wavelengths are 1250 nm for x-polarization and 1080 nm for y-polarization. Additionally, the peak confinement losses at the resonant wavelengths are 97.04 and 12.89 dB/cm for x-and y-polarizations, respectively. As the operating wavelength, red/blue shifts far from the resonant wavelength, and the confinement loss approaches its tail from the peak loss. From Figure 3, it is noted that at the resonant condition, energy transmission increases significantly from the core to the SP for the x-polarized field compared with the y-polarized field because of efficient excitation of metal electrons by the evanescent wave. As a result, we consider sensor optical characteristics for x-polarization.

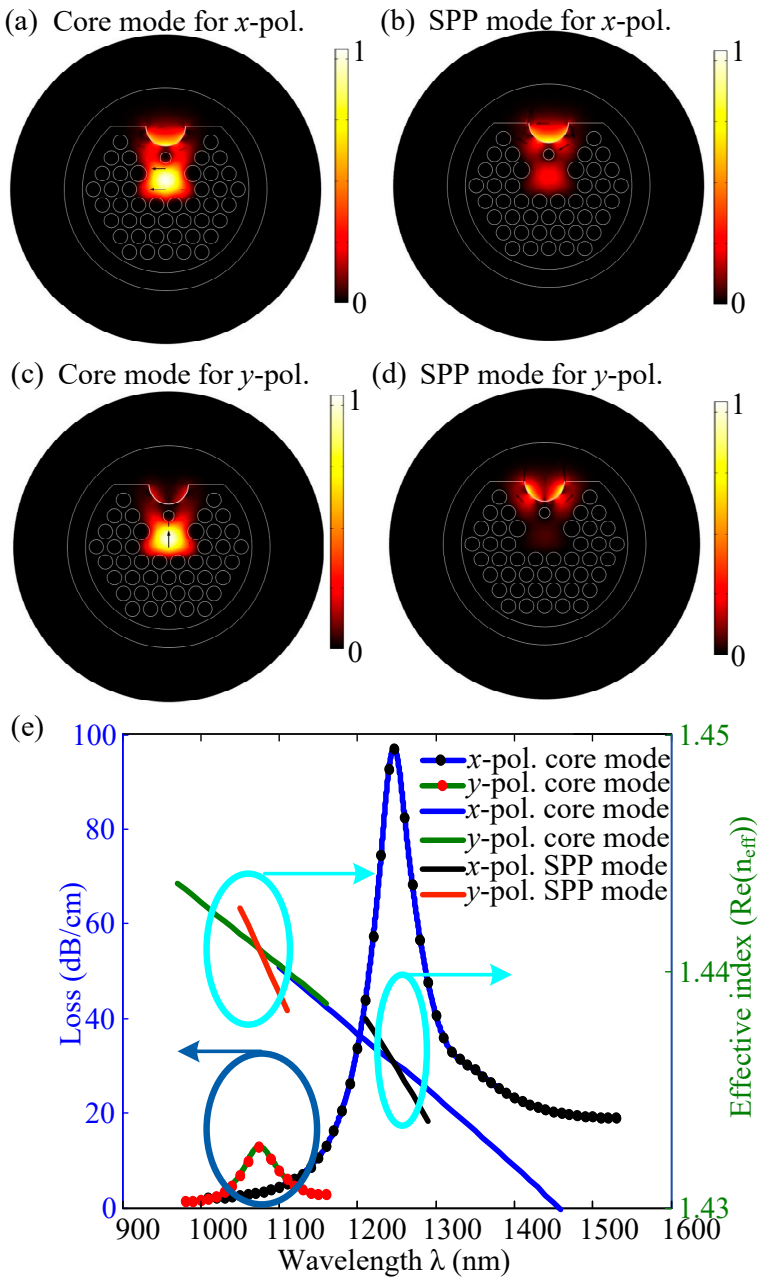

Figure 3. Electric field distribution of *x*-polarized (**a**) core, (**b**) SPP mode, *y*-polarized (**c**) core, and (**d**) SPP mode; (**e**)confinement loss spectrum for both *x*- and *y*-polarization as a function of wavelength for analyte RI of 1.43; dispersion relation of core and SPP mode for both *x*- and *y*-polarization.

The propagation loss spectra of the *x*-polarized fundamental mode are shown in Figure 4a due to the medium placed in the channel with RI ranging from 1.33 to 1.44. The increase in the analyte RI results in the reduction in core-cladding index contrast; as a result, resonant wavelength redshifts and peak confinement loss raises. The resonant wavelengths and peak confinement losses are shown in Table 1 for different analyte RI. The loss spectrum for higher analyte RI (e.g., 1.44) shows multiple resonance peaks at longer wavelengths similar to the Ref. in [38], where only the largest peak loss is considered to find the resonant wavelength. The higher peak loss is considered due to larger energy transmission from the core mode to SPP mode compared with the other subpeaks.

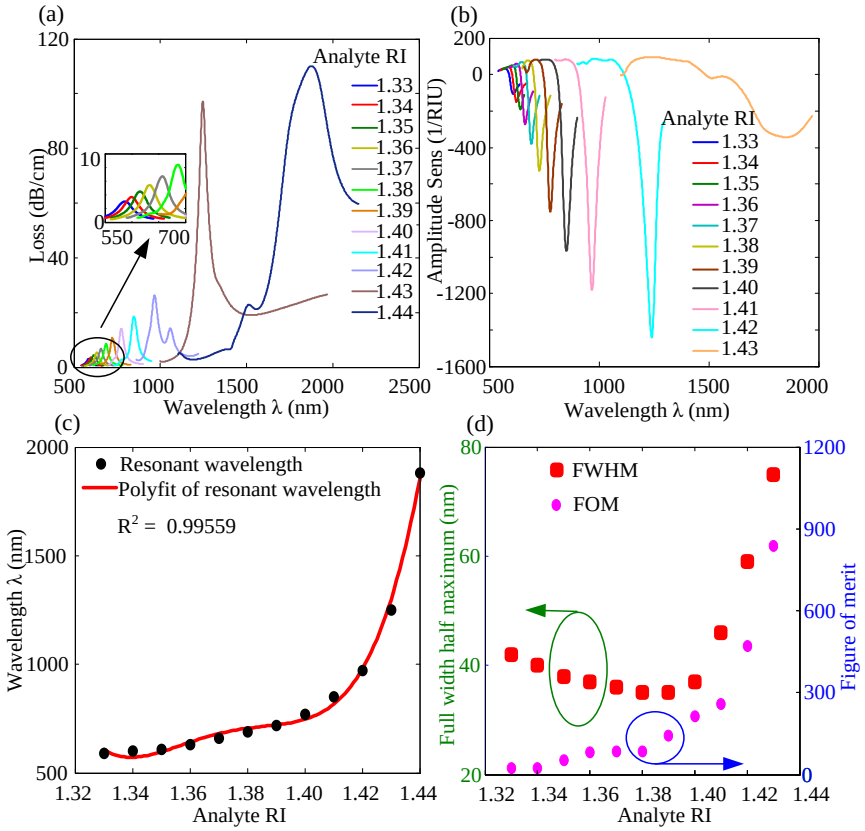

Figure 4. Sensor characteristics for analyte RI ranging from 1.33 to 1.44: (**a**)confinement loss as a function of wavelength, (**b**)different analytes' amplitude sensitivity as a function of wavelength, (**c**)resonant wavelength and their polynomial fitting as a function of analyte RI, and (**d**) FWHM and FOM as a function of analyte RI.

Table 1. Performance of sensor for analyte RI from 1.33 to 1.44.

RI	$\lambda_{res.}$	α_{peak}	S_λ	Resolution	S_A	FWHM	FOM
	nm	dB/cm	nm/RIU	RIU	RIU^{-1}	nm	
1.33	590	3.05	1000	1.00×10^{-04}	106.64	42	24
1.34	600	3.70	1000	1.00×10^{-04}	145.89	40	25
1.35	610	4.42	2000	5.00×10^{-05}	194.74	38	52
1.36	630	5.43	3000	3.33×10^{-05}	272.29	37	82
1.37	660	6.72	3000	3.33×10^{-05}	381.55	36	84
1.38	690	8.40	3000	3.33×10^{-05}	529.83	35	85
1.39	720	10.85	5000	2.00×10^{-05}	751.41	35	142
1.40	770	14.21	8000	1.25×10^{-05}	968.03	37	215
1.41	850	18.58	12,000	8.33×10^{-05}	1182.50	46	259
1.42	970	26.26	28,000	3.57×10^{-06}	1439.00	59	471
1.43	1250	97.04	63,000	1.59×10^{-06}	343.59	75	839
1.44	1880	110.07	NA	NA	NA	NA	NA

The increase in analyte RI results in the redshift of the resonant wavelengths that are used to find the wavelength sensitivity by the following equation

$$S_\lambda(\text{nm/RIU}) = \Delta\lambda_{\text{resonance}}(n_a)/\Delta n_a \quad (5)$$

where $\Delta\lambda_{\text{resonance}}$ is the amount of redshift of the resonant wavelengths in nm for the difference of analyte RI of Δn_a [11]. Since Δn_a = 0.01 is constant in our analysis, wavelength sensitivity S_λ shows higher values for larger $\Delta\lambda_{\text{resonance}}$. For example, the resonant wavelength changes from 590 nm to 600 nm as n_a changes from 1.33 to 1.34, which results in the wavelength sensitivity of 1000 nm/RIU. Similarly, for the increase in n_a from 1.43 to 1.44, the change of $\lambda_{\text{resonance}}$ is maximum (i.e., from 1250 nm to 1880 nm), which leads to the maximum wavelength sensitivity of 63,000 nm/RIU. The wavelength sensitivities are listed in Table 1 for other analytes' RI.

The sensitivity parameter termed as the resolution of a sensor detects the minimum change in RI and can be found as follows:

$$R_\lambda(\text{RIU}) = \Delta n_a \times \Delta\lambda_{\text{min}}/\Delta\lambda_{\text{resonance}} \quad (6)$$

where $\Delta\lambda_{\text{min}} = 0.1$ nm is the minimum spectral resolution [11]. Table 1 shows sensor resolutions for analytes' RI from 1.33 to 1.43. The Table 1 shows that as analyte RI changes from 1.43 to 1.44, the sensor resolution is minimum (i.e., 1.59×10^{-06} RIU), corresponding to the highest wavelength sensitivity of 63,000 nm/RIU. The smallest resolution 1.59×10^{-06} RIU in Table 1 indicates the detector's ability to discriminate between analytes' RI that are close enough.

There is another important sensor parameter known as amplitude sensitivity, which is measured by the amplitude interrogation method. The amplitude sensitivity analysis is a low-cost sensitivity measurement process compared with wavelength sensitivity because this method does not engage spectral manipulation. The amplitude sensitivity is defined as below:

$$S_A(\text{RIU}^{-1}) = -\frac{1}{\alpha(\lambda, n_a)}\frac{\partial\alpha(\lambda, n_a)}{\partial n_a} \quad (7)$$

where $\alpha(\lambda, n_a)$ is confinement loss for analyte RI of n_a at a particular wavelength λ. $\partial\alpha(\lambda, n_a)$ indicates change in propagation loss at wavelength λ for ∂n_a change in analyte RI [11]. The amplitude sensitivity depends only on $\partial\alpha(\lambda, n_a)$ and $\alpha(\lambda, n_a)$ because $\partial n_a = 0.01$ in our analysis. Figure 4b shows the amplitude sensitivity spectra of different analytes' RI varying from 1.33 to 1.43. The maximum amplitude sensitivity increases gradually with the increase in the analyte RI from 1.33 to 1.42. Such as, for the increase in analyte RI from 1.33 to 1.34 (i.e., $\partial n_a = 0.01$), the maximum amplitude sensitivity is found as 106.64 RIU^{-1} and the change in RI from 1.34 to 1.35 (i.e., $\partial n_a = 0.01$) results in the maximum amplitude sensitivity of 145.89 RIU^{-1}. However, the maximum amplitude sensitivity decreases form 1439.00 RIU^{-1} to 343.59 RIU^{-1} with the change in the analyte RI from 1.43 to 1.44. Table 1 shows peak amplitude sensitivities for analytes' RI from 1.33 to 1.43. Table 1 shows that the highest amplitude sensitivity is 1439.00 RIU^{-1} with a resolution of 6.94×10^{-06} RIU for change in analyte RI from 1.42 to 1.43.

The resonant wavelengths for different analytes' RI in the range of 1.33 to 1.44 and the polynomial fitting are shown in Figure 4c. From resonant wavelengths, it is found that the R-squared value of the sensor is close to unity (i.e., R^2 = 0.99559), which indicates the sensor is highly linear. The full width at half maximum (FWHM) is found from the loss spectra of different analyte RI and plotted in Figure 4d and shown in Table 1. The FWHM decreases with the increase in the analyte RI and reaches a minimum for RI = 1.39 and increases again with the increase in analyte RI. The FWHM is used to characterize the sensor in terms of the figure of merit (FOM), which is a ratio of wavelength sensitivity to the FWHM. Figure 4d shows that FOM increases with the increase in the analyte RI. The highest FOM is 839 for analyte RI = 1.43 as shown in Table 1.

4. The Effect of Structural Parameters

Since the thickness of the plasmonic layer controls the mode coupling between the core and SPP mode, the performance of the sensor is affected by this parameter, as shown in Figure 5. Loss spectra of analyte RIs 1.34 and 1.35 are shown in Figure 5a for the gold thickness of 30, 40, and 50 nm. As the gold thickness increases, the peak loss component decreases due to the decrease in the depth of penetration of the electric field in the metal layer. For example, peak losses are 7.10, 4.42, and 2.36 dB/cm for the gold thickness of 30, 40, and 50 nm, respectively, in the case of RI = 1.35. The change in loss spectra affects the amplitude sensitivity and FWHM as shown in Figure 5b in the case of analyte RI of 1.34. From Figure 5b, it is seen that amplitude sensitivity reaches a maximum for the gold thickness of 40 nm. However, the FWHM is found to be minimum for the gold thickness of 40 nm. The change in gold thickness hardly affects the wavelength sensitivity; therefore, FOM (i.e., FOM = 25.21 in the case of analyte RI = 1.34) must have the highest magnitude at the gold thickness of 40 nm.

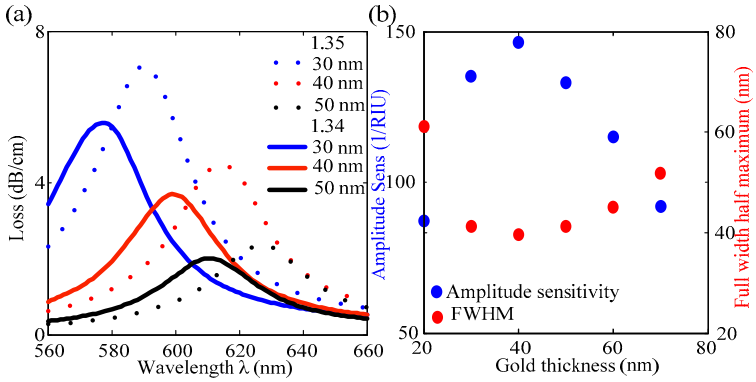

Figure 5. Effect of gold layer thickness: (**a**)loss spectra for analyte RI of 1.34, and 1.35, and (**b**)amplitude sensitivity and FWHM as a function of gold layer thickness for analyte RI = 1.34.

To determine the effect of thickness of the adhesive layer on the sensing performance, loss spectra are shown in Figure 6a for analyte RI of 1.33, 1.34, and 1.35. The penetration of electrical waves decreases with the increase in metal thickness. Therefore, in all cases of analyte RIs, the peak confinement loss increases with the decrease in the adhesive layer thickness. For example, the peak losses are 4.16, 4.22, and 4.62 dB/cm for analyte RI = 1.35 in the case of TiO_2 thicknesses of 8, 6, and 4 nm, respectively. The amplitude sensitivities also altered due to the change in loss spectra. However, the effect of the TiO_2 layer on the sensitivity is not significant. For example, for analyte RI of 1.34, the maximum amplitude sensitivities are 143.04, 145.89, and 146.21 RIU^{-1} for the TiO_2 layer of 4, 6, and 8 nm.

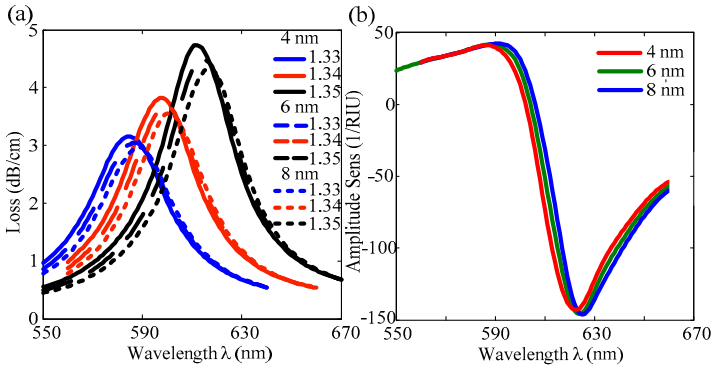

Figure 6. Effect of adhesive layer thickness: change in (**a**) loss spectra for analyte RI of 1.33, 1.34, and 1.35, and (**b**) amplitude sensitivity with the increase in TiO_2 layer for analyte RI = 1.34.

The distance between the semicircular-shaped channel and the core of the PCF is fixed in this sensor. However, the distance between the channel and the core of the PCF can be changed by varying the diameter of the channel. For the increase in channel diameter by +10%, the distance between the core and plasmonic layer decreases by −10%, which leads to the easy coupling between the core mode and SPP mode. As a result, energy shifts significantly from the core to the SPP mode, and the peak loss increases as shown in Figure 7a. However, the resonant wavelength remains constant for the change in the channel size within ±10% of the d_{ch}. Additionally, as the channel dimension decreases from the optimum value, there is no significant change in the energy transfer of the core mode to the plasmonic mode, as shown in Figure 7a. The channel dimension affects only the amplitude sensitivity, as shown in Figure 7b. From Figure 7b, it is found that the amplitude sensitivity is larger for the optimum channel size d_{ch}, and other values of d_{ch} result in lower amplitude sensitivities.

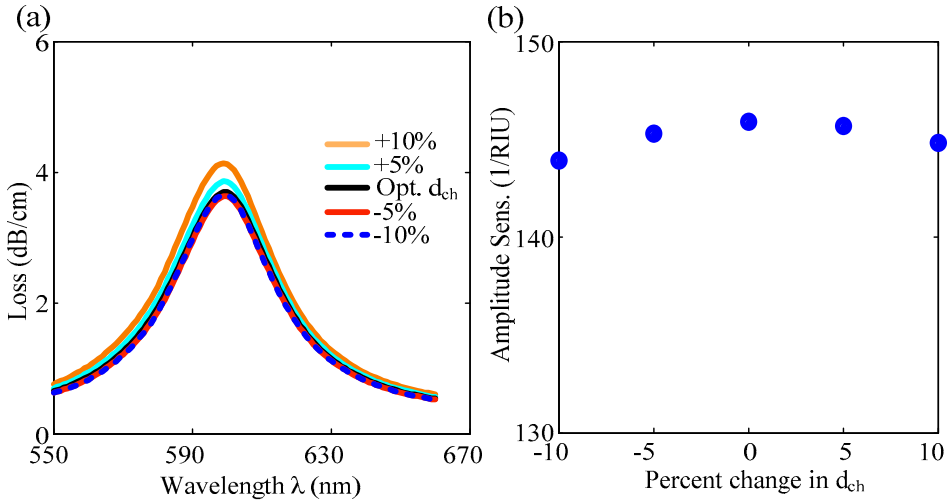

Figure 7. Effect of external channel size: (**a**) loss spectra for different value of d_{ch}, and (**b**) amplitude sensitivities as a function of the percent change in d_{ch}.

In Figure 8, the effects of sensor structural parameters on the maximum wavelength sensitivity and sensing range are further explored. Figure 8a shows that as the air hole diameter d_1 increases beyond 0.6Λ, the sensing range raises to 1.44 from 1.43. The wavelength sensitivity S_λ increases significantly to 50,000 nm/RIU for $d_1 = 0.6\Lambda$, and a further increase in d_1 results in the gradual increment of S_λ. From Figure 8b, it is found that S_λ is maximum only for $d_s = 0.6\Lambda$, and the sensing range remains constant at 1.44 for $d_s \geq 0.6\Lambda$. The sensing range and S_λ decrease with the decrease in d_s. Even in the absence of the air hole with diameter d_s, the maximum sensing range becomes 1.42. The effect of outer channel diameter d_{ch} is shown in Figure 8c. The maximum sensing range of 1.44 is obtained for $d_{ch} \geq 1.9\Lambda$, and the maximum S_λ is found at $d_{ch} = 2.1\Lambda$. For $d_{ch} = 2.2\Lambda$, the maximum S_λ decreases only 3% from the maximum S_λ found at $d_{ch} = 2.1\Lambda$. The structural parameter d has no effect on the maximum sensing range for the values of d from 0.3 Λ to 0.9 Λ, as shown in Figure 8d. However, the maximum S_λ increases gradually with the increase in d. Figure 8e shows that the maximum sensitivity and sensing range is larger for the optimum pitch size of 2 μm.

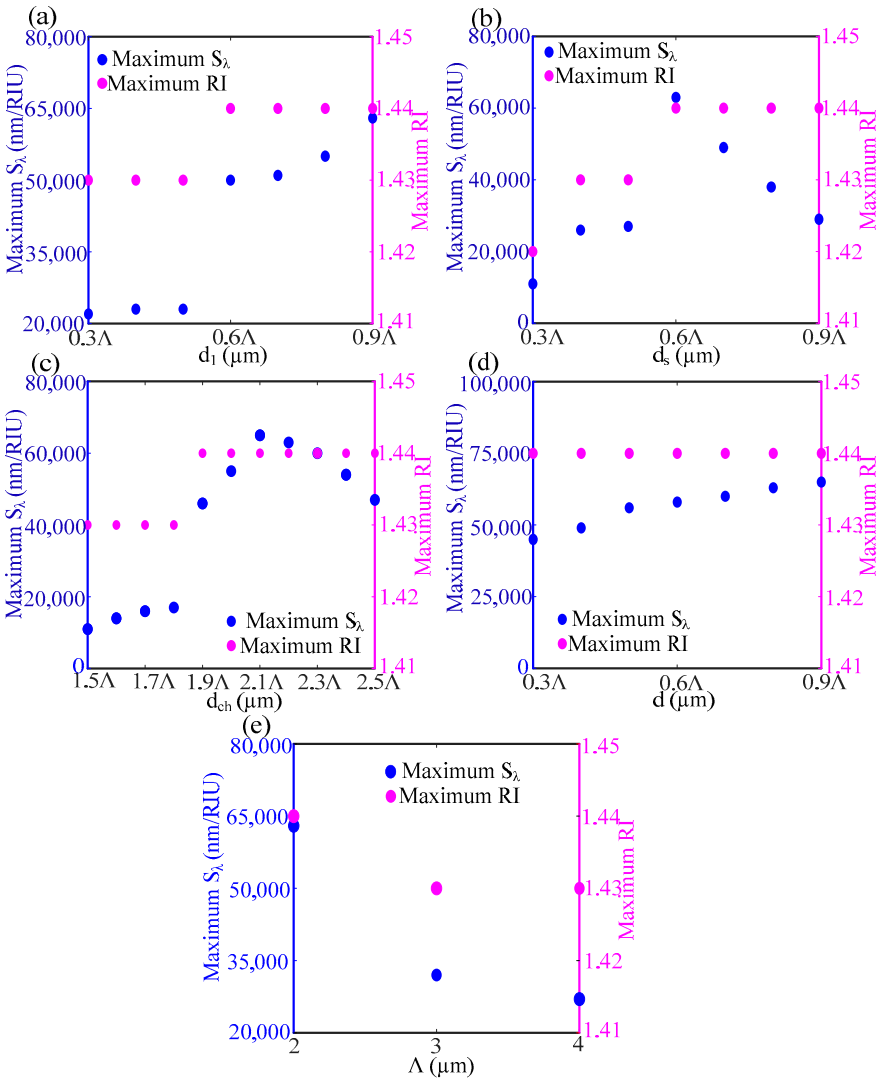

Figure 8. Effect of (**a**) air-hole diameter d_1, (**b**) air-hole diameter d_s, (**c**) outer-channel diameter d_{ch}, and (**d**) air-hole diameter d, and (**e**) pitch on maximum wavelength sensitivity and sensing range.

To investigate fabrication tolerance, the dependence of the sensing parameters is examined by varying all the structural parameters of the PCF sensor within ±10% of the optimized value. Figure 9a,b shows loss spectra and amplitude sensitivity, respectively, for the change in pitch. All air hole diameters depend on the pitch, so a reduction in pitch results in the opening of the leakage path. Therefore, a reduced pitch leads to an increment of confinement loss and vice versa. For example, as the pitch is reduced by −10%, the peak loss increases by about 40%. Since the resonant wavelength remains unchanged, the wavelength sensitivity stays unaffected by the change in pitch. However, the amplitude sensitivities are altered significantly by the alteration in pitch. For example, the amplitude sensitivity increases by 1.48% for the increase in pitch by +10%. Another structural parameter d_s plays an important role in the sensing performance, as shown in Figure 9c,d. The air hole diameter d_s regulates the evanescent wave that interacts with the plasmonic material. The smaller size of ds leads to a larger leakage path and more light to interact with the analyte. Thus, the energy transfer increases from the fundamental modes to the plasmonic modes for the reduction in ds. For example, the peak loss at the resonant wavelength rises by 36% from the optimum due to the −10% decrease in d_s. Additionally, the amplitude sensitivity increases by only 0.72% for the −10% decreases in d_s. However, the wavelength sensitivities are unchanged due to the change in d_s, similar to the case of pitch change. The effect of air hole diameter d is shown in Figure 9e,f, and that of air hole

diameter d_1 is shown in Figure 9g,h. As one can see from Figure 9e–h, the effect of the change in parameters d and d_1 is not significant because these parameters can hardly affect the leakage path. Therefore, peak loss and the resonant wavelength are almost the same, which leads to no noteworthy change in the wavelength and amplitude sensitivities.

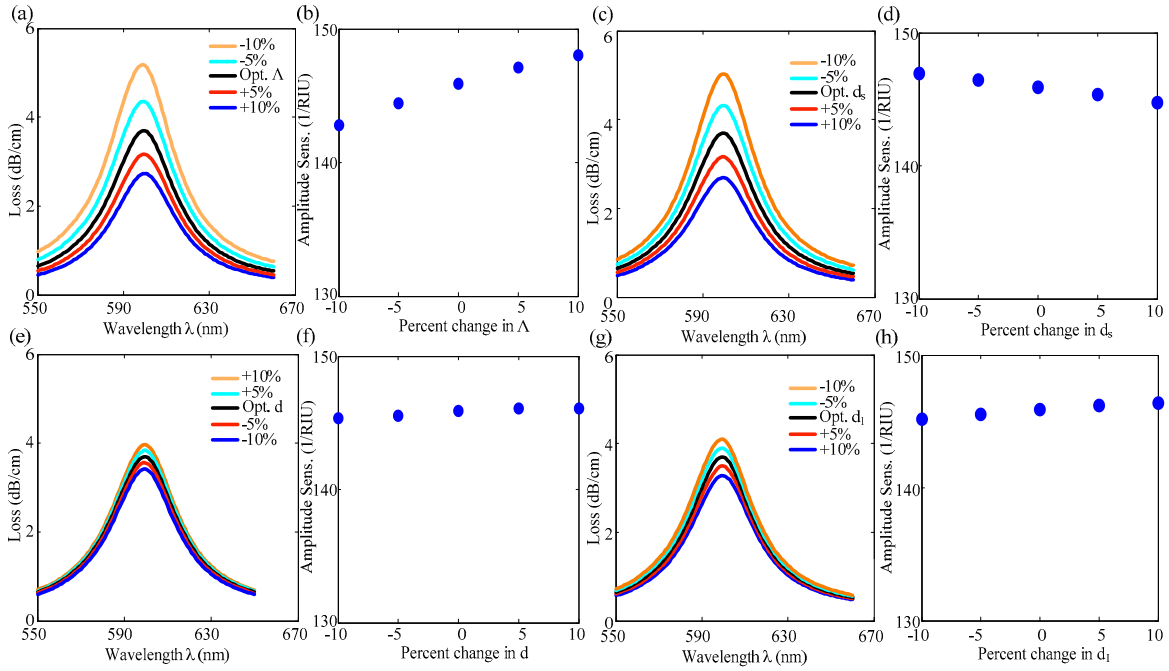

Figure 9. Investigation of the sensor's structural parameters for analyte RI = 1.34. Effect of pitch Λ: (**a**) loss spectra (**b**) amplitude sensitivity, and effect of air-hole diameter d_s: (**c**) loss spectra, (**d**) amplitude sensitivity, and effect of air-hole diameter d: (**e**) loss spectra, (**f**) amplitude sensitivity, and effect of air-hole diameter d_1: (**g**) loss spectra and (**h**) amplitude sensitivity.

Different open channel-based PCF sensors are available where the plasmonic layer is deposited either on the curved surface or flat surface of D-shaped sensors [39]. In some cases, a microchannel is produced in PCF by a complex milling process [40]. To avoid the complex fabrication process of the open channel, a large air hole is inserted in the stack preform of PCF that has a hexagonal lattice structure. We compare the performance analysis of those previously reported PCFs with the proposed open channel-based PCF sensor in Table 2. The sensor performance is analyzed in terms of maximum wavelength sensitivity, amplitude sensitivity, wavelength resolution, and FOM. The proposed sensor not only shows better performance but also eliminates the complex fabrication process. The structural parameters considered in the model are compatible with the fabrication process of the sensor by using the stack-and-draw fiber drawing technique. The fabrication tolerance investigation shows that structural parameter variations within ±10% of their optimized value barely affect the wavelength and amplitude sensitivities. It is noteworthy that a fiber can be fabricated for structural parameter variation within ±1%. The robust performance with a high sensitivity enables the sensor for biomedical application in the sensing range of RI from 1.33 to 1.44.

Table 2. Performance evaluation of existing open channel sensors in terms of sensing parameters with the proposed sensor.

Ref.	Structure	RI	S_λ	S_A	Resolution	FOM
			nm/RIU	RIU^{-1}	RIU	
[12]	Open-ring channel D-shaped PCF sensor with hexagonal lattice	1.20–1.29	11,055	NA	9.05×10^{-6}	NA
[20]	Hollow core D-shaped sensor	1.33–1.34	2900	120	NA	NA
[22]	Hollow core as microchannel in D-shaped sensor	1.37–1.41	12,780	5059	3.36×10^{-6}	1282
[40]	AZO Coated Microchannel	1.32–1.34	5000	167	2.00×10^{-5}	NA
[41]	Microchannel-based D-shaped PCF sensor with octagonal lattice	1.26–1.36	11,039	NA	9.06×10^{-6}	NA
[42]	Two micro-openings D-shaped PCF sensor	1.31–1.37	11,750	NA	8.51×10^{-6}	NA
This work	Semicircle channel D-shaped PCF sensor	1.33–1.44	63,000	1439	1.59×10^{-06}	839

5. Conclusions

In this paper, a modified D-shaped PCF-based plasmonic sensor with a larger semicircular open channel is proposed to detect RI from 1.33 to 1.44. Plasmonic material is applied inside the smooth inner surface of the semicircular-shaped channel rather than on the flat surface of an ordinary D-shaped sensor to avoid surface roughness. A large semicircular-shaped channel helps the easy coating of the plasmonic film with quick infiltration by the analyte to be detected and effortless cleaning of the channel. This unique design improves the coupling between fundamental and SPP modes by reducing the separation between the plasmonic layer and the solid core, which results in higher sensitivity. It is found numerically that the sensor has a high spectral sensitivity of 63,000 nm/RIU with a resolution of 1.59×10^{-06} RIU and an amplitude sensitivity of 1439 RIU^{-1} with a resolution of 6.94×10^{-06} RIU. Additionally, the sensor is highly linear with an R-squared value of 0.99559, and the FOM of the sensor is 839.

Author Contributions: Conceptualization, J.M.N. and T.A.; writing—original draft preparation, J.M.N.; writing—review and editing, T.A., M.A.H., J.A. and N.H.H.; supervision, T.A. All authors have read and agreed to the published version of the manuscript.

Funding: This research received no external funding.

Institutional Review Board Statement: Not applicable.

Informed Consent Statement: Not applicable.

Data Availability Statement: The data are generated using COMSOL Multiphysics software. The raw data are available from the corresponding author on reasonable request.

Conflicts of Interest: The authors declare no conflict of interest.

References

1. Peng, L.; Shi, F.; Zhou, G.; Ge, S.; Hou, Z.; Xia, C.A. Surface Plasmon Biosensor Based on a D-Shaped Microstructured Optical FiberWith Rectangular Lattice. *IEEE Photonics J.* **2015**, *7*, 1–9. [CrossRef]
2. Gauvreau, B.; Hassani, A.; Fehri, M.F.; Kabashin, A.; Skorobogatiy, M. Photonic bandgap fiber-based Surface Plasmon Resonance sensors. *Opt. Express* **2007**, *15*, 11413–11426. [CrossRef] [PubMed]
3. Guo, T. Fiber Grating-Assisted Surface Plasmon Resonance for Biochemical and Electrochemical Sensing. *J. Lightwave Technol.* **2018**, *35*, 3323–3333. [CrossRef]
4. Mishra, S.K.; Tripathi, D.C.; Mishra, A.K. Metallic grating-assisted fiber optic SPR sensor with extreme sensitivity in IR region. *Plasmonics* **2021**, *17*, 575–579. [CrossRef]

5. Mishra, S.K.; Mishra, A.K. ITO/Polymer matrix assisted surface plasmon resonance based fiber optic sensor. *Results Opt.* **2021**, *5*, 100173. [CrossRef]
6. Zhao, L.; Han, H.; Luan, N.; Liu, J.; Song, L.; Hu, Y. A temperature plasmonic sensor based on a side opening hollow fiber filled with high refractive index sensing medium. *Sensors* **2019**, *19*, 3730. [CrossRef]
7. Wang, F.; Sun, Z.; Liu, C.; Sun, T.; Chu, P.K. A high-sensitivity photonic crystal fiber (PCF) based on the surface plasmon resonance (SPR) biosensor for detection of density alteration in non-physiological cells (DANCE). *Opto-Electron. Rev.* **2018**, *26*, 50–56. [CrossRef]
8. Yasli, A. Cancer Detection with Surface Plasmon Resonance-Based Photonic Crystal Fiber Biosensor. *Plasmonics* **2021**, *16*, 1605–1612. [CrossRef]
9. Liu, Y.; Li, S.; Chen, H.; Li, J.; Zhang, W.; Wang, M. Surface Plasmon Resonance Induced High Sensitivity Temperature and Refractive Index Sensor Based on Evanescent Field Enhanced Photonic Crystal Fiber. *J. Lightwave Technol.* **2019**, *38*, 919–928. [CrossRef]
10. Haider, F.; Mashrafi, M.; Aoni, R.A.; Haider, R.; Hossen, M.; Ahmed, T.; Mahdiraji, G.A.; Ahmed, R. Multi-Analyte Detection Based on Integrated Internal and External Sensing Approach. *IEEE Trans. Nanobioscience* **2021**, *21*, 29–36. [CrossRef]
11. Ahmed, T.; Paul, A.K.; Anower, M.S.; Razzak, S.A. Surface plasmon resonance biosensor based on hexagonal lattice dual-core photonic crystal fiber. *Appl. Opt.* **2019**, *58*, 8416–8422. [CrossRef] [PubMed]
12. Chen, X.; Xia, L.; Li, C. Surface Plasmon Resonance Sensor Based on a Novel D-Shaped Photonic Crystal Fiber for Low Refractive Index Detection. *IEEE Photonics J.* **2018**, *10*, 1–9. [CrossRef]
13. Ahmed, T.; Haider, F.; Aoni, R.A.; Ahmed, R. Highly Sensitive U-Shaped Micro-channel Photonic Crystal Fiber–Based Plasmonic Biosensor. *Plasmonics* **2021**, *16*, 2215–2223. [CrossRef]
14. West, P.R.; Ishii, S.; Naik, G.V.; Emani, N.K.; Shalaev, V.M.; Boltasseva, A. Searching for better plasmonic materials. *Laser Photonics Rev.* **2010**, *4*, 795–808. [CrossRef]
15. Dash, J.N.; Jha, R. SPR Biosensor Based on Polymer PCF Coated With Conducting Metal Oxide. *IEEE Photonics Technol. Lett.* **2014**, *26*, 595–598. [CrossRef]
16. Li, C.; Song, B.; Guo, Y.; Wu, J.; Huang, W.; Wu, X.; Jin, C.; Chen, S. Two Modes Excited SPR Sensor Employing Gold-Coated Photonic Crystal Fiber Based on Three-Layers Air-Holes. *IEEE Sens. J.* **2020**, *20*, 5893–5899. [CrossRef]
17. Silla, E.; Arnau, A.; TuñóN, I. Fundamental Principles Governing Solvents Use. In *Handbook of Solvents*; Wypych, G., Ed.; Chem Tec Publishing: Toronto, ON, Canada, 2014; pp. 1–72. [CrossRef]
18. Bolin, F.P.; Preuss, L.E.; Taylor, R.C.; Ference, R.J. Refractive index of some mammalian tissues using a fiber optic cladding method. *Appl. Opt.* **1989**, *28*, 2297–2303. [CrossRef]
19. Chen, Y.; Xie, Q.; Li, X.; Zhou, H.; Hong, X.; Geng, Y. Experimental realization of D-shaped photonic crystal fiber SPR sensor. *J. Phys. D Appl. Phys.* **2016**, *50*, 25101. [CrossRef]
20. Luan, N.; Wang, R.; Lv, W.; Yao, J. Surface plasmon resonance sensor based on D-shaped microstructured optical fiber with hollow core. *Opt. Express* **2015**, *23*, 8576–8582. [CrossRef]
21. Gupta, A.; Singh, H.; Singh, A.; Singh, R.K.; Tiwari, A. D-Shaped photonic crystal fiber–based surface plasmon resonance biosensors with spatially distributed bimetallic layers. *Plasmonics* **2020**, *15*, 1323–1330. [CrossRef]
22. Guo, Y.; Li, J.; Wang, X.; Zhang, S.; Liu, Y.; Wang, J.; Wang, S.; Meng, X.; Hao, R.; Li, S. Highly sensitive sensor based on D-shaped microstructure fiber with hollow core. *Opt. Laser Technol.* **2020**, *123*, 105922. [CrossRef]
23. Liu, C.; Yang, L.; Lu, X.; Liu, Q.; Wang, F.; Lv, J.; Sun, T.; Mu, H.; Chu, P.K. Mid-infrared surface plasmon resonance sensor based on photonic crystal fibers. *Opt. Express* **2017**, *25*, 14227–14237. [CrossRef] [PubMed]
24. Yang, X.; Lu, Y.; Wang, M.; Yao, J. An exposed-core grapefruit fibers based surface plasmon resonance sensor. *Sensors* **2015**, *15*, 17106–17114. [CrossRef] [PubMed]
25. Yang, X.; Lu, Y.; Liu, B.; Yao, J. Simulation of LSPR sensor based on exposed-core grapefruit fiber with a silver nanoshell. *J. Lightwave Technol.* **2017**, *35*, 4728–4733. [CrossRef]
26. Yang, X.; Lu, Y.; Wang, M.; Yao, J. SPR sensor based on exposed-core grapefruit fiber with bimetallic structure. *IEEE Photonics Technol. Lett.* **2015**, *28*, 649–652. [CrossRef]
27. Gómez-Cardona, N.D.; Reyes-Vera, E.; Torres, P. Multi-plasmon resonances in microstructured optical fibers: Extending the detection range of SPR sensors and a multi-analyte sensing technique. *IEEE Sens. J.* **2018**, *18*, 7492–7498. [CrossRef]
28. Cardona, N. High sensitivity refractive index sensor based on excitation of long range surface plasmon polaritons in H-shaped fiber. *Sensors* **2019**, *20*, 2111. [CrossRef]
29. Gonzalez-Valencia, E.; Herrera, R.A.; Torres, P. Bloch surface wave resonance in photonic crystal fibers: Towards ultra-wide range refractive index sensors. *Opt. Express* **2019**, *27*, 8236–8245. [CrossRef]
30. Akowuah, E.K.; Gorman, T.; Ademgil, H.; Haxha, S.; Robinson, G.K.; Oliver, J.V. Numerical Analysis of a Photonic Crystal Fiber for Biosensing Applications. *IEEE J. Quantum Electron.* **2012**, *48*, 1403–1410. [CrossRef]
31. Wiederhecker, G.S.; Cordeiro, C.M.B.; Couny, F.; Benabid, F.; Maier, S.A.; Knight, J.C.; Cruz, C.H.B.; Fragnito, H.L. Field enhancement within an optical fibre with a subwavelength air core. *Nat. Photonics* **2007**, *1*, 115–118. [CrossRef]
32. Byun, D.; Jin, Y.; Kim, B.; Lee, J.K.; Park, D. Photocatalytic TiO2 deposition bychemical vapor deposition. *J. Hazard. Mater.* **2000**, *73*, 199–206. [CrossRef]

33. Dominik, M.; Leśniewski, A.; Janczuk, M.; Niedziółka-Jönsson, J.; Hołdyński, M.; Godlewski, M.; Bock, W.J.; Śmietana, M. Titanium oxide thin films obtained with physical and chemical vapour deposition methods for optical biosensing purposes. *Biosens. Bioelectron.* **2017**, *93*, 102–109. [CrossRef] [PubMed]
34. Schwuchow, A.; Zobel, M.; Csaki, A.; Schröder, K.; Kobelke, J.; Fritzsche, W.; Schuster, K. Monolayers of different metal nanoparticles in microstructured optical fibers with multiplexplasmonic properties. *Opt. Mater. Express* **2012**, *2*, 1050–1055. [CrossRef]
35. Boehm, J.; François, A.; Ebendorff-Heidepriem, H.; Monro, T.M. Chemical Deposition of Silver for the Fabrication of Surface Plasmon Microstructured Optical Fibre Sensors. *Plasmonics* **2011**, *6*, 133–136. [CrossRef]
36. Vial, A.; Grimault, A.S.; Macías, D.; Barchiesi, D.; De La Chapelle, M.L. Improved analyticalfit of gold dispersion: Application to the modeling of extinction spectra with a finitedifference time-domain method. *Phys. Review. B Condens. Matter Mater. Phys.* **2005**, *71*, 085416. [CrossRef]
37. DeVore, J.R. Refractive Indices of Rutile and Sphalerite. *J. Opt. Soc. Am.* **1951**, *41*, 416–419. [CrossRef]
38. Chu, S.; Nakkeeran, K.; Abobaker, A.M.; Aphale, S.S.; Sivabalan, S.; Ramesh Babu, P.; Senthilnathan, K. Influence of the Sub-Peak of Secondary Surface Plasmon Resonance Onto the Sensing Performance of a D-Shaped Photonic Crystal Fibre Sensor. *IEEE Sens. J.* **2021**, *21*, 33–42. [CrossRef]
39. Singh, S.; Prajapati, Y.K. Highly sensitive dual-core symmetrical side-polished modified Dshaped SPR based PCF refractive index sensor with deeply etched micro openings. *Optik* **2021**, *235*, 166657. [CrossRef]
40. Dash, J.N.; Das, R.; Jha, R. AZO Coated Microchannel Incorporated PCF-Based SPR Sensor: A Numerical Analysis. *IEEE Photonics Technol. Lett.* **2018**, *30*, 1032–1035. [CrossRef]
41. Zhang, S.; Li, J.; Li, S. Design and numerical analysis of a novel dual-polarized refractive index sensor based on D-shaped photonic crystal fiber. *Metrologia* **2018**, *55*, 828–839. [CrossRef]
42. Zhang, S.; Li, J.; Li, S.; Liu, Q.; Wu, J.; Guo, Y. Surface plasmon resonance sensor based on D shaped photonic crystal fiber with two micro-openings. *J. Phys. D Appl.* **2018**, *51*, 305104. [CrossRef]